Spectral Element Methods for Transitional Flows

Paul F. Fischer,[1] Gerald W. Kruse,[2] and Francis Loth[3]

Abstract

We describe the development and implementation of an efficient spectral element code for simulating transitional flows in complex three-dimensional domains. Critical to this effort is the use of geometrically nonconforming elements that allow localized refinement in regions of interest, coupled with a stabilized high-order time-split formulation of the semi-discrete Navier-Stokes equations. Simulations of transition in a model of an arteriovenous graft illustrate the potential of this approach in biomechanical applications.

1 Introduction

Simulation of transitional flow in complex geometries poses significant numerical challenges. Even in simple geometries, such as plane-Poiseuille flow, the transition process can be more difficult to simulate than turbulent flow at the same Reynolds number [34]. Proper identification of the point of transition (in both physical and parameter space) calls for accurate representation of the convective operator such that numerical dissipation and dispersion do not overwhelm physical effects. Because small-scale structures are transported with minimal physical dissipation, accurate long-time integration is required. These challenges can be efficiently addressed though the use of high-order methods in space and time. The presence of small-scale structures also implies a need for significant spatial resolution in supercritical regions, which may be localized in space. Nonconforming meshes allow for local refinement in these regions without undue spatial resolution throughout the domain.

[1] Mathematics and Computer Science Division, Argonne National Laboratory, Argonne, IL 60439.

[2] Dept. of Mathematics and Computer Science, Juniata College, Huntingdon, PA 16652.

[3] Mechanical Engineering Dept., University of Illinois, Chicago, IL 60607.

We consider a nonconforming spectral element method for solution of the incompressible Navier-Stokes equations in $\mathbb{R}^d$,

$$\frac{\partial \mathbf{u}}{\partial t} + \mathbf{u} \cdot \nabla \mathbf{u} \;=\; -\nabla p \;+\; \frac{1}{Re}\nabla^2 \mathbf{u} \;\text{ in } \Omega, \quad \nabla \cdot \mathbf{u} \;=\; 0 \;\text{ in } \Omega, \tag{1}$$

with prescribed boundary and initial conditions for the velocity, $\mathbf{u}$. Here, p is the pressure and $Re = \frac{UL}{\nu}$ the Reynolds number based on characteristic velocity and length scales. Spatial discretization of (1) is based on the $\mathbb{P}_N - \mathbb{P}_{N-2}$ spectral element method (SEM) [23], which uses compatible velocity and pressure spaces that are free of spurious modes. This is coupled with high-order operator splitting methods to yield a sequence of symmetric positive definite (SPD) subproblems to be solved at each timestep. Convection-dominated problems are stabilized by using a recently developed filtering procedure [14]. The method attains exponential convergence in space and second- or third-order accuracy in time.

The paper is organized as follows. Section 2 provides an overview of the spectral element method and the time advancement scheme. Section 3 discusses the filter-based stabilization. Section 4 describes the nonconforming implementation. Simulation results for transitional flow in an arteriovenous graft model are presented in Section 5, and a brief conclusion is given in Section 6.

2 Navier-Stokes Discretization

The temporal discretization of the Navier-Stokes equations is based on the high-order operator-splitting methods developed in [24]. The convective term is expressed as a material derivative, which is discretized by using a stable mth-order backward-difference scheme, m=2 or 3. For m=2 we have

$$\frac{\tilde{\mathbf{u}}^{n-2} - 4\tilde{\mathbf{u}}^{n-1} + 3\tilde{\mathbf{u}}}{2\Delta t} = S(\tilde{\mathbf{u}}) \,,$$

where $S(\tilde{\mathbf{u}})$ is the linear symmetric Stokes problem to be solved implicitly, and $\tilde{\mathbf{u}}^{n-q}$ is a velocity field that is computed as the explicit solution to a pure convection problem over the interval $[t^{n-q}, t^n]$. The subintegration of the convection term permits values of Δt corresponding to convective Courant numbers of 1–5, thus significantly reducing the number of (expensive) Stokes solves.

The Stokes discretization is based on the variational form *Find* $(\tilde{\mathbf{u}}, p) \in X_N \times Y_N$ *such that*

$$\frac{1}{Re}(\nabla \tilde{\mathbf{u}}, \nabla \mathbf{v})_{GL} + \frac{3}{2\Delta t}(\tilde{\mathbf{u}}, \mathbf{v})_{GL} - (p, \nabla \cdot \mathbf{v})_G \quad = \quad (\mathbf{f}, \mathbf{v})_{GL}, \tag{2}$$

$$(\nabla \cdot \tilde{\mathbf{u}}, q)_G \quad = \quad 0,$$

$\forall\, (\mathbf{v}, q) \in X_N \times Y_N$. The inner products $(.,.)_{GL}$ and $(.,.)_G$ refer to the Gauss-Lobatto-Legendre (GL) and Gauss-Legendre (G) quadratures associated with the spaces $X_N := [Z_N \cap H_0^1(\Omega)]^d$ and $Y_N := Z_{N-2}$, respectively. Here, $Z_N := \{v \in L^2(\Omega) | v_{|\Omega^k} \in \mathbb{P}_N(\Omega^k)\}$, where L^2 is the space of square integrable functions on Ω; H_0^1 is the space of functions in L^2 that vanish on the boundary and whose first derivative is also in L^2; and $\mathbb{P}_N(\Omega^k)$ is the space of functions on element Ω^k whose image is a tensor-product polynomial of degree $\leq N$ in the reference domain, $\hat{\Omega} := [-1,1]^d$. For $d = 2$, a typical element in X_N is written

$$\tilde{\mathbf{u}}(\mathbf{x}^k(r,s))\big|_{\Omega^k} \;=\; \sum_{i=0}^{N} \sum_{j=0}^{N} \tilde{\mathbf{u}}_{ij}^k h_i^N(r) h_j^N(s)\,, \tag{3}$$

where $\tilde{\mathbf{u}}_{ij}^k$ is the nodal basis coefficient; $h_i^N \in \mathbb{P}_N$ is the Lagrange polynomial based on the GL quadrature points, $\{\xi_j^N\}_{j=0}^N$ (the zeros of $(1-\xi^2)L'_N(\xi)$, where L_N is the Legendre polynomial of degree N); and $\mathbf{x}^k(r,s)$ is the coordinate mapping from $\hat{\Omega}$ to Ω^k. For Y_N, a tensor-product form similar to (3) is used, save that the interpolants are based on the G points since interelement continuity is not enforced.

We assume that $\Omega = \cup_{k=1}^K \Omega^k$ and that, for the conforming case, $\Gamma^{kl} := \bar{\Omega}^k \cap \bar{\Omega}^l$ for $k \neq l$ is void, a single vertex, or an entire edge. For the nonconforming case, Γ^{kl} may be a subset of either $\partial\Omega^k$ or $\partial\Omega^l$ but must coincide with an entire edge of one of the elements. Function continuity ($\tilde{\mathbf{u}} \in H^1$) is enforced by matching the Lagrangian basis functions on subdomain interfaces. The velocity space is thus conforming, even for the nonconforming meshes, as described in Section 4.

Insertion of the SEM basis into (2) yields a discrete Stokes system to be solved at each step:

$$H\,\underline{\tilde{\mathbf{u}}} - D^T\,\underline{p}^n = B\,\underline{\mathbf{f}}^n, \quad D\,\underline{\tilde{\mathbf{u}}} = 0. \tag{4}$$

Here, $H = \frac{1}{Re}A + \frac{1}{\Delta t}B$ is the discrete equivalent of the Helmholtz operator, $(-\frac{1}{Re}\nabla^2 + \frac{1}{\Delta t})$; $-A$ is the discrete Laplacian; B is the (diagonal) mass matrix associated with the velocity mesh; D is the discrete divergence operator, and $\underline{\mathbf{f}}^n$ accounts for the explicit treatment of the nonlinear terms. A filter is applied to $\tilde{\mathbf{u}}$ to yield the solution $\mathbf{u}^n$ at time level $t^n := n\Delta t$. Note that the Galerkin approach implies that the governing system in (4) is symmetric and that the matrices H, A, and B are all symmetric positive definite.

The Stokes system (4) is treated by an mth-order operator splitting analyzed in [24, 28]. The splitting is applied to the *discretized* system so

that ad hoc boundary conditions are avoided. For $m = 2$, one first solves

$$H\,\hat{\underline{\mathbf{u}}} = B\,\underline{\mathbf{f}}^n + D^T\,\underline{p}^n, \tag{5}$$

which is followed by a pressure correction step

$$E\delta\underline{p} = -D\hat{\underline{\mathbf{u}}}, \qquad \tilde{\underline{\mathbf{u}}} = \hat{\underline{\mathbf{u}}} + \Delta t B^{-1} D^T \delta\underline{p} + O(\Delta t^2), \tag{6}$$

where $E := \Delta t D B^{-1} D^T$ is the Stokes Schur complement governing the pressure in the absence of the viscous term. For $m > 2$, higher-order extrapolation for $\underline{p}$ must be used in (5).

To close this section, we summarize our Navier-Stokes time advancement scheme. We begin with an explicit convective update involving several steps small enough to satisfy the CFL condition. This is followed by Jacobi-preconditioned conjugate gradient (PCG) solution of d Helmholtz problems (5), which for large Re and small Δt are strongly diagonally dominant and therefore well conditioned. Next, we solve the Poisson-like system for the pressure (6) using PCG. The pressure preconditioner is based on the overlapping Schwarz procedure of Dryja and Widlund [10] and is described in detail in [12, 13]. The pressure solve is the most computationally intensive step. To accelerate convergence, we generate a high-quality initial guess for $\delta\underline{p}$ by computing its projection onto the space of previous solutions [11]. Finally, we obtain the solution at time level n by filtering the intermediate velocity field,

$$\underline{\mathbf{u}}^n = F_\alpha \tilde{\underline{\mathbf{u}}}, \tag{7}$$

As described in the next section, the filter provides stability in high-Reynolds number applications.

3 Filtering

One of principal attractions of spectral element methods is that, for smooth solutions, the error decreases exponentially fast with increasing polynomial degree N (see Table 1). However, spectral element methods can also be highly effective in solving transport problems in which the solution is *not* smooth. This property is illustrated by the convected-cone example of Fig. 1, which was introduced by Gottlieb and Orszag [16]. A unit-height cone with a base-radius of 0.1 centered at (x, y)=(0,.25) is subjected to plane rotation in the domain $\Omega = [0, 1]^2$. The solution is evolved according to $u_t + \mathbf{c} \cdot \nabla u = 0$, with periodic boundary conditions and convecting field $\mathbf{c} = (y - .5, .5 - x)$. Figure 1 shows the results after a single revolution for three spectral element discretizations, (K, N), where K is the number of

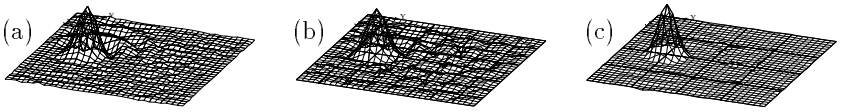

Figure 1: Spectral element results for convected cone problem [16] on 32×32 grids: (a) $(K,N) = (256,2)$, (b) $(64,4)$, (c) $(16,8)$.

(square) elements, and N is the polynomial degree in each spatial direction. Each case corresponds to a 32×32 grid. Time-stepping is based on third-order Adams-Bashforth (AB3) with $\Delta t = \pi/1000$. (Fourth-order Runge-Kutta results are identical.) The low-order cases (N=2, 4) show evidence of significant numerical dispersion. By contrast, the dispersion is diminished for the moderately high-order case ($N = 8$), and the solution produces a reasonable representation of the original cone. The minima for the three respective cases are $-.1419$, $-.1127$, and $-.0371$, while the maxima are .7693, .7413, and .8652.

Unfortunately, Galerkin formulations suffer from well-known instabilities in convection-dominated flows when underresolved boundary layers are encountered. A classic example is the one-dimensional steady convection-diffusion problem $u_x - \nu u_{xx} = f$, $u(-1)$=$u(1)$=0, f=1. The spectral Galerkin formulation of this problem is *Find* $u \in \mathbb{P}_N^0$ *such that*

$$(u_x - \nu u_{xx} - f, v) = 0 \;\; \forall v \in \mathbb{P}_N^0 \,,$$

where $\mathbb{P}_N^0$ is the space of all polynomials of degree $\leq N$ vanishing at ±1 and $(.,.)$ is the standard L^2 inner-product on $[-1,1]$. As shown by Canuto [7], and illustrated in Fig. 2, the spectral solution is unbounded as $\nu \to 0$ when N is even. As shown in Fig. 2b, for large ν (smooth solutions), the error is smaller for $N = 16$ than for $N = 15$. However, as $\nu \to 0$, the error grows without bound for N=16 but remains bounded for N=15.

Ideally, one would like to retain the good transport properties illustrated in Fig. 1, without the sensitivity to parameters exemplified in Fig. 2. Several proposed strategies for stabilizing convection-dominated problems involve a reformulation of the Galerkin procedure, for example, Petrov-Galerkin schemes [29], shifted grids [15], the addition of bubble functions [8], or the addition of higher-order derivative terms, such as in the spectrally vanishing viscosity method [32, 25]. Related to this last approach are filtering schemes [5, 17]. A significant advantage of filtering is that it can be applied as a postprocessing step and therefore does not require changing the underlying discretization or solver. In particular, solvers designed for symmetric systems continue to be useful.

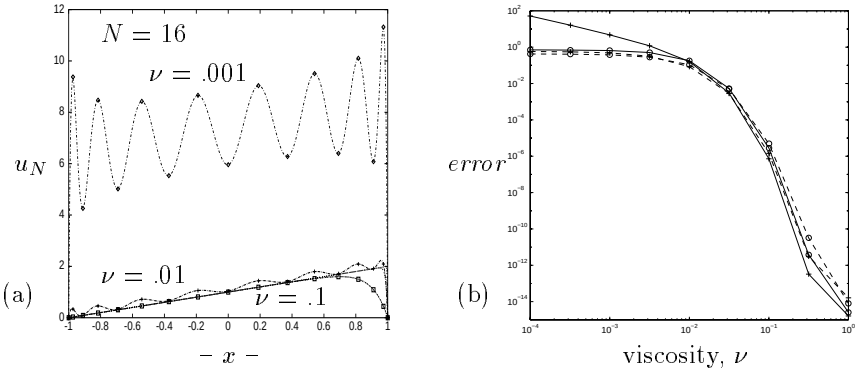

Figure 2: Spectral Galerkin results for steady advection-diffusion problem: (a) $u_N(x)$ for $N = 16$, $\nu = .001$–$.1$, (b) maximum pointwise error with (- - -) and without (——) filtering for $N = 15$ ($\circ$) and $N = 16$ (+).

As pointed out by Boyd [5], a special basis is required for the SEM in order to preserve interelement continuity. In [14], we introduced an interpolation-based filtering procedure that can be applied on an element-by-element basis. The local operator is constructed as follows. Let I_N^M be the matrix having entries

$$\left(I_N^M\right)_{ij} = h_j^N(\xi_i^M).$$

The action of I_N^M is to interpolate a Lagrange polynomial on $[-1,1]$ from the order-N GL points to the order-M GL points, ξ_i^M. This operator is stable both in L^2 and H^1 norms (that are natural norms for this problem) as can be found in [4] (13.27–28). Similarly, the matrix $\Pi_{N-1} := I_{N-1}^N I_N^{N-1}$ defines a projector from $\mathbb{P}_N$ to $\mathbb{P}_{N-1}$ on $[-1,1]$. The matrix that implements the one-dimensional filter on $[-1,1]$ is defined by

$$\hat{F}_\alpha \;:=\; \alpha\Pi_{N-1} \;+\; (1-\alpha)I\,.$$

In higher space dimensions, one uses the tensor-product form $F_\alpha := \hat{F}_\alpha \otimes \ldots \otimes \hat{F}_\alpha$ within each element. The interpolation-based procedure ensures that interelement continuity is preserved and, because the interpolation error for smooth u is exponentially small as $N \to \infty$, that spectral accuracy is not compromised. Because the nodal basis points ξ_i^N interlace ξ_i^{N-1}, F_α tends to dampen high-frequency oscillations. One can apply the filter intermittently rather than on each time step. However, we prefer to control the filter strength through the single parameter α, which is typically taken to be 0.05. Note that $\alpha = 1$ corresponds to a full projection onto $\mathbb{P}_{N-1}$, effectively yielding a sharp cut-off in modal space, whereas $0 < \alpha < 1$ yields a smoother decay, which is known to be preferable when filtering [5, 17, 25].

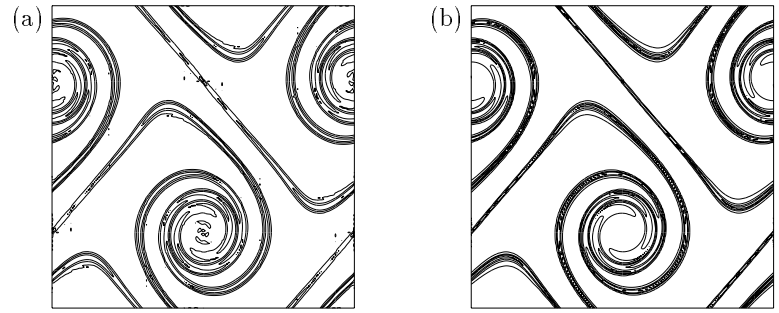

Figure 3: Vorticity contours from -70 to 70 by 140/15 for shear-layer rollup problem with ρ=30, $Re = 10^5$: (a) $K = 256, N = 8$, (b) $K = 256, N = 16$.

Examples We illustrate the effect of the filter on several example problems, starting with the shear layer roll-up problem studied in [6]. Equation (1) is solved on $\Omega := [0,1]^2$ with doubly periodic boundary conditions and initial condition

$$u = \begin{cases} \tanh(\rho(y-0.25)) & \text{for } y \le 0.5 \\ \tanh(\rho(0.75-y)) & \text{for } y > 0.5 \end{cases}, \quad v = 0.05\sin(2\pi x),$$

which corresponds to a pair of nearly parallel shear layers of thickness $O(1/\rho)$. For any fixed mesh, the initial shear layers are drawn thinner until their thickness is below the resolvable scale. The problem is solved by using the SEM on a 16×16 array of elements with N=4, 8, 16, and 32, and timestep size $\Delta t = .002$. Without filtering (α=0), the solution is unstable for all N considered and blows up at $t^* < 1.0$. With the filter, the simulation can continue indefinitely. Filtered results (α=0.3) at $t = 1.5$ are shown in Fig. 3. Further results are presented in [14].

As a second example, we examine the errors in computed growth rates when the least stable eigenmode for the Orr-Sommerfeld equation is superimposed on plane Poiseuille channel flow at $Re = 7500$, following [12]. The amplitude of the perturbation is 10^{-5}, implying that the nonlinear Navier-Stokes results can be compared with linear theory to about five significant

Table 1: Spatial and Temporal Convergence, Orr-Sommerfeld Problem

	$\Delta t = 0.00325$		$N = 17$	2nd-Order		3rd-Order	
N	$\alpha = 0.$	$\alpha = .2$	Δt	$\alpha = 0.$	$\alpha = .2$	$\alpha = 0.$	$\alpha = .2$
7	0.2364	0.2745	0.200	0.1262	0.1262	171.37	0.0207
9	0.0017	0.1193	0.100	0.0347	0.0347	0.0027	0.0027
11	0.0046	0.0111	0.050	0.0091	0.0091	161.13	0.0004
13	0.0001	0.0007	0.025	0.0024	0.0024	1.0446	0.0001

digits. The errors (see (41) in [12]) at time $t = 60$ given in Table 1 reveal exponential convergence in N for both the filtered and unfiltered cases. It is also clear that $O(\Delta t^2)$ and $O(\Delta t^3)$ convergence is obtained for the filtered case but that the unfiltered results are unstable for the third-order scheme. In this case, the stability provided by the filter permits the use of higher-order temporal schemes, thereby allowing a larger time step for a given accuracy.

Finally, we revisit the instability encountered in the example of Fig. 2 by considering the effects of the filter when the solution to the unsteady convection-diffusion equation, $u_t + u_x - \nu u_{xx} = f$, $u(-1)=u(1)=0$, $f=1$, is evolved to steady state. Discretization by the SEM in space and by Crank-Nicholson and third-order Adams-Bashforth for the respective diffusive and convective terms in time leads to the system

$$H\underline{\tilde{u}} = H_R\underline{u}^n + C(\frac{23}{12}\underline{u}^n - \frac{16}{12}\underline{u}^{n-1} + \frac{5}{12}\underline{u}^{n-2}) + B\underline{f}\,, \quad \underline{u}^{n+1} = F_\alpha\underline{\tilde{u}}\,, \quad (8)$$

where $H = (\frac{\nu}{2}A + \frac{1}{\Delta t}B)$ and $H_R = (-\frac{\nu}{2}A + \frac{1}{\Delta t}B)$ are discrete Helmholtz operators and C is the convection operator. The fixed point of (8) satisfies

$$\left(-\nu A + C + H(F_\alpha^{-1} - I)\right)\underline{u} = B\underline{f}\,. \quad (9)$$

The Δt dependence in (9) can be eliminated by assuming that $1 \simeq \mathrm{CFL} := \Delta t/\Delta x \simeq \Delta t N^2$.

For any Galerkin formulation, C is skew symmetric and therefore singular if the number of variables is odd (the spurious mode being $L_N - L_0$). The eigenvalues of $(F_\alpha^{-1} - I)$ are $\{0, 0, \ldots, 0, \frac{\alpha}{1-\alpha}\}$ (the nonzero eigenmode being $\phi_N(x) := \frac{2N-1}{N(N-1)}(1-x^2)L'_{N-1}(x) = L_N - L_{N-2}$). By suppressing the unstable mode, the stabilizing term, $H(F_\alpha^{-1} - I)$, prevents (9) from blowing up as $\nu \to 0$. The dashed line in Fig. 2b shows the effect of the filter for $N = 15$ and 16. For moderate to large ν, the error behavior is essentially the same as for the unfiltered case, while for small ν the solution is stable for each value of N.

We note that ϕ_N corresponds to a single element in the filter basis suggested by Boyd [5]. One can easily suppress more elements in this basis in order to construct smoother filters, as suggested, for example, in [5, 25]. However, our early experiences and asymptotic analysis ($\nu \to 0$ in (9)) indicate that slight suppression of just the Nth mode is sufficient to stabilize the $\mathbb{P}_N - \mathbb{P}_{N-2}$ method at moderate to high Reynolds numbers.

4 Nonconforming Spectral Elements

Element-by-element operator evaluation is central to the efficiency of the SEM because it allows the use of tensor-product forms, which reduce the work and storage complexity from $O(KN^{2d})$ to $O(KN^{d+1})$ and $O(KN^d)$, respectively [27]. The extension to nonconforming spaces preserves this feature and essentially involves redefining in the interface operators that impose the matching conditions across element interfaces. Here, we consider the development of interpolation-based interface conditions that leave the approximation spaces X^N and Y^N unchanged but allow for nonconforming meshes of the type illustrated in Fig. 4a. On the the nonconforming interface Γ we refer to the large element as the parent element, the two (or more) smaller elements as children, and the interface between them as a parent-child (PC) interface. We do not restrict the number of child elements per PC edge. However, we insist that the union of the closure of the child faces constitutes the closure of the parent face. While this restriction rules out configurations such as shown in Fig. 4b, it allows us to preserve local (*element-to-element*) interactions. For similar reasons, we also exclude configurations in which the endpoint of one PC interface connects to the interior of another, as shown in Fig. 4c.

Much work has been done on nonconforming spectral element methods, starting with the early work of Mavriplis [26], Anagnostou et al. [1], and others [3, 18, 9]. Most of these have employed "mortar" elements that increase flexibility through the use of L^2-projection operators to enforce weak continuity at the nonconforming interface. In particular, the "vertex-free" mortar spaces of Ben Belgacem and Maday [3] alleviate the restriction of Fig. 4c. The conforming-space/nonconforming-mesh approach used here was motivated by the results of Rønquist [30], who reported spurious eigenvalues in the convection operator for certain combinations of convection and nonconforming formulations. For brevity, in this article, *conforming* will

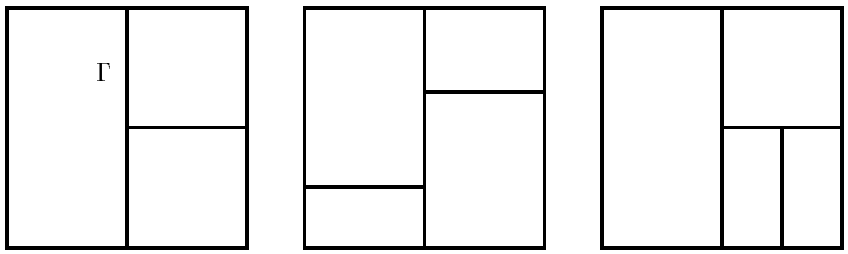

Figure 4: (a) Valid and (b,c) invalid nonconforming meshes in $\mathbb{R}^2$.

refer to conforming meshes (no hanging vertices), and *nonconforming* will refer to conforming spaces with nonconforming meshes. We further assume that the polynomial degree N is the same in each spectral element.

To introduce the interface matching conditions, we begin by considering enforcement of continuity of a function $u(\mathbf{x})$, $\mathbf{x} \in \Omega \subset \mathbb{R}^2$ for the conforming case. For isoparametrically mapped elements, the geometry within each element is represented in a form similar to (3), that is,

$$\mathbf{x}^k(r,s)\big|_{\Omega^k} \;=\; \sum_{i=0}^{N}\sum_{j=0}^{N} \mathbf{x}_{ij}^k h_i^N(r) h_j^N(s)\;. \tag{10}$$

Because the basis functions are Lagrangian, function continuity for $u(\mathbf{x})$ is enforced by simply equating coincident nodal values, that is,

$$\mathbf{x}_{ij}^k = \mathbf{x}_{\hat{i}\hat{j}}^{\hat{k}} \Longrightarrow u_{ij}^k = u_{\hat{i}\hat{j}}^{\hat{k}}. \tag{11}$$

If n is the number of distinct nodes on Ω, then (11) represents $K(N+1)^d - n$ constraints on the set of local nodal values $\{u_{ij}^k\}$.

It is convenient for notational purposes to cast the constraint (11) in matrix form. Let $\underline{u} \in \mathbb{R}^n$ denote the vector of nodal values associated with a global numbering of the distinct nodes in all of Ω, as illustrated in Fig. 5a. Let $\underline{u}^k \in \mathbb{R}^{(N+1)^d}$ denote the vector of local basis coefficients associated with Ω^k:

$$\underline{u}^k \quad := \quad \left(u_{00}^k, u_{10}^k, \ldots, u_{NN}^k\right)^T \;, \qquad k = 1, \ldots, K,$$

as illustrated in Fig. 5b, and let $\underline{u}_L$ be the $K(N+1)^d \times 1$ collection of these local vectors. If u is to be continuous, then there exists a Boolean connectivity matrix, Q, that maps the global form $\underline{u}$ to its local counterpart $\underline{u}_L$ such that (11) is satisfied. The operation

$$\underline{u}_L \;=\; Q\underline{u} \tag{12}$$

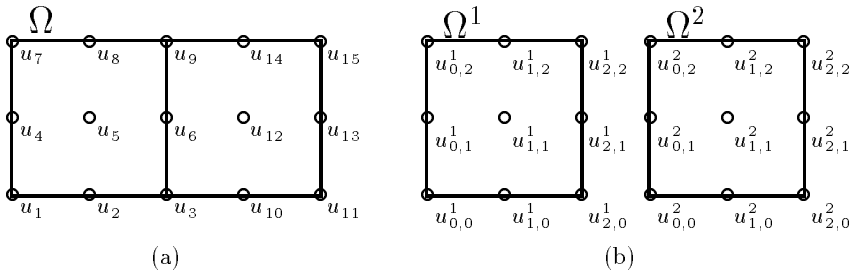

Figure 5: (a) Global and (b) local numbering for spectral element mesh.

is referred to as a *scatter* from the global ($\underline{u}$) to local ($\underline{u}_L$) vector. For example, in Fig. 5 the global value u_3 is copied to local coefficients $u^1_{2,0}$ and $u^2_{0,0}$. Note that for every global vector, $\underline{u}$, there is a corresponding local vector, $\underline{u}_L$, given by (12). The converse is not true because Q is not invertible. However, we will frequently employ the closely related *gather* operation

$$\underline{v} \;=\; Q^T \underline{u}_L \tag{13}$$

and denote the output ($\underline{v}$) with a different notation from the input ($\underline{u}_L$). Whereas the action of Q is to *copy* entries of $\underline{u}$ to $\underline{u}_L$, the action of Q^T is to *sum* entries from corresponding nodes. In practice, the matrix Q is never constructed. Rather, the *actions* of Q and Q^T are implemented via indirect addressing (and message passing, in parallel implementations). The combined gather-scatter operation $\Sigma' := QQ^T$ is often referred to as *direct stiffness summation* in the spectral element literature.

We illustrate the use of the above notation by considering an integral that arises in the weak formulation of the Poisson equation. Assuming u, $v \in H^1$, we have

$$\int_\Omega \nabla u \cdot \nabla v \, dV \;=\; \sum_{k=1}^{K} \int_{\Omega^k} \nabla u \cdot \nabla v \, dV. \tag{14}$$

Restricting u and v to X^N, inserting the SEM basis (3), and substituting GL quadrature for integration, we obtain

$$\int_{\Omega^k} \nabla u \cdot \nabla v \, dV \;\simeq\; (\underline{v}^k)^T A^k \underline{u}^k \,, \tag{15}$$

where A^k is the local elemental stiffness matrix and the approximation ($\simeq$) results from substitution of quadrature for integration. An example of A^k is given by the tensor-product form

$$A^k \;=\; \frac{L^k_s}{L^k_r} \left(\widehat{B} \otimes \widehat{A} \right) \;+\; \frac{L^k_r}{L^k_s} \left(\widehat{A} \otimes \widehat{B} \right),$$

for the case where Ω^k is an $L^k_r \times L^k_s$ rectangle. Here, $\widehat{A}$ and $\widehat{B}$ are the respective stiffness and mass matrices on $[-1, 1]$, with entries

$$\widehat{A}_{ij} \;=\; \sum_{l=0}^{N} \widehat{D}_{li} \rho_l \widehat{D}_{lj} \,, \;=\; (\widehat{D}^T \widehat{B} \widehat{D})_{ij}, \qquad \widehat{B}_{ij} \;=\; \rho_i \delta_{ij} \;=\; \delta_{ij} \int_{-1}^{1} h^N_i(r) dr,$$

where ρ_i is the GL quadrature weight, $\widehat{D}_{ij} = h^{N\prime}_j(\xi^N_i)$ is the one-dimensional derivative matrix, and δ_{ij} is the Kronecker delta. Substituting (15) into

(14) yields

$$\int_\Omega \nabla u \cdot \nabla v \, dV \;=\; \sum_{k=1}^{K} (\underline{v}^k)^T A^k \underline{u}^k \;=\; \underline{v}_L^T A_L \underline{u}_L \;=\; \underline{v}^T Q^T A_L Q \underline{u}, \qquad (16)$$

where $A_L := \textit{block-diag}(A^k)$ comprises the unassembled local stiffness matrices. Note that the final equality is a result of the interface matching conditions, u, $v \in H^1$.

Equation (16) illustrates how the matrix assembly process (Q, Q^T) is decoupled from the local spectral element operators contained in A_L. In the nonconforming case, Q must be modified at the PC interfaces, where global nodal values are stored along the parent edge. Application of Q involves interpolation of the associated Lagrange polynomial to nodal points distributed along the corresponding child faces. To ease parallelism, we implement this using the two-step process illustrated in Fig. 6a. Data is first copied from the parent data structure to the corresponding child edges.

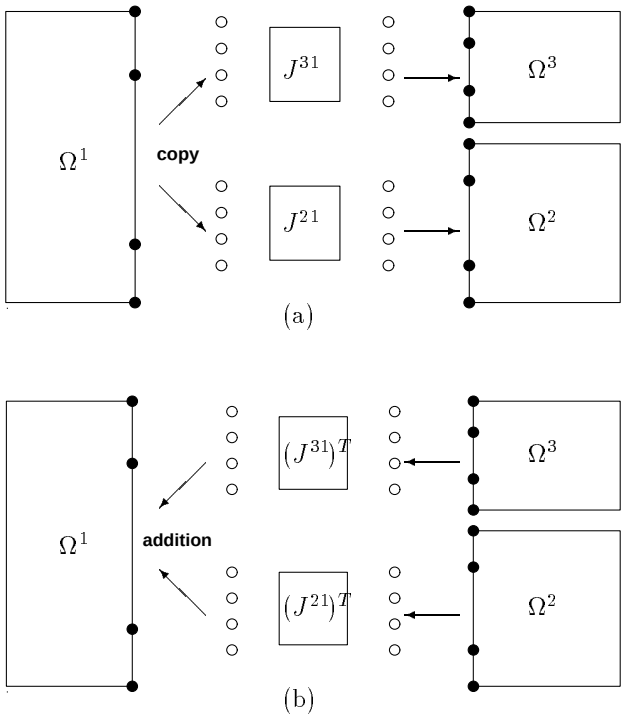

Figure 6: Schematic of (a) Q and (b) Q^T implementation.

This step may involve communication if the parent and child elements are not on the same processor. After the copy, an interpolation operator, J^{cp}, is locally applied to produce the desired nodal values on the child face. This two-step procedure can be represented in matrix form as

$$Q = J_L \tilde{Q},$$

where $\tilde{Q}$ is a Boolean matrix similar to the Q operator used in the conforming case, and J_L is block-diagonal and comprises local matrices J^{cp} that interpolate from $\partial\Omega^p$ to $\partial\Omega^p \cap \partial\Omega^c$. The entries of J^{cp} are

$$(J^{cp})_{ij} = h_j^N(\zeta_i^{cp}),$$

where ζ_i^{cp} represents the mapping of the GL points from the child edge to its parent. In $\mathbb{R}^3$, the local interpolation operators mapping from the parent to child face have the tensor-product form $J_s^{cp} \otimes J_r^{cp}$. Application of Q^T follows in the reverse order, with summation replacing the copy, as illustrated in Fig. 6b.

For time advancement of the incompressible Navier-Stokes equations, it is desirable to have a diagonal mass matrix [18]. If ψ_i, ψ_j are two elements of the Lagrangian basis set spanning X^N, the entries of the mass matrix for the standard spectral element formulation are $B_{ij} := (\psi_i, \psi_j)_{GL}$. Equivalently, we have $B = Q^T B_L Q$, where $B_L := \textit{block-diag}(B^k)$ comprises the local mass matrices. For the two-dimensional case, an entry of B^k for a nodal point $\mathbf{x}_{pq}^k$ is simply $\rho_p \rho_q \mathcal{J}_{pq}^k$, where $\mathcal{J}_{pq}^k$ is the Jacobian associated with the mapping $\hat{\Omega} \rightarrow \Omega^k$. Diagonality of the mass matrix in the conforming case is assured because of the coincidence of the quadrature points and the Lagrangian nodal points. In the nonconforming case, this property does not hold because the nodal basis functions along the parent edge do not coincide with the quadrature points along the child edge. However, a diagonal (lumped) mass matrix $\tilde{B}$ can be recovered by setting

$$\underline{\tilde{b}} \;:=\; B\underline{\hat{e}} \;=\; Q^T B_L \underline{\hat{e}}_L \tag{17}$$

and then setting $\tilde{B}_{ij} = \delta_{ij}\underline{\tilde{b}}_i$. Here, $\underline{\hat{e}}$ and $\underline{\hat{e}}_L$ are the respective global and local vectors containing all ones. Note that, because B_L is diagonal, (17) amounts to applying Q^T to the local vector $\underline{b}_L$ containing the entries of B_L. In [20] it was shown that this mass lumping procedure is equivalent to replacing the more accurate quadrature in the child elements by quadrature at the nodal points along the parent edge.

Conditioning. The nonconforming discretization is particularly effective for external flow problems. In addition to reducing the number of gridpoints in the far field, it allows one to avoid the creation of high-aspect ratio elements

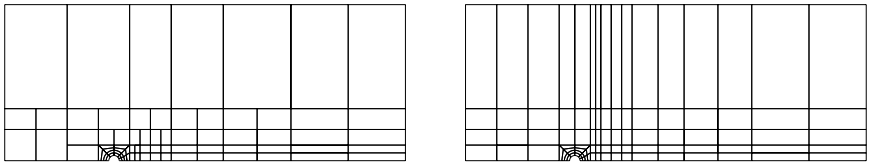

Figure 7: K=77 noncforming (left) and $K = 93$ conforming (right) meshes for cylinder problem.

that can lead to ill-conditioning [12]. This point is illustrated by the two-dimensional meshes in Fig. 7, which are used to solve the problem of start-up flow past a cylinder at $Re = 5000$, following [12, 13]. The conforming mesh (left) exhibits a few high-aspect ratio elements in the far field that have been eliminated in the nonconforming mesh (right). Table 2 shows the number of Schwarz PCG iterations to reduce the pressure residual on the first timestep by 10^{-5} for the case $N = 7$ and two successive quad-refinements of the meshes in Fig. 7. The conforming case shows a marked increase in iteration count with refinement. In contrast, the nonconforming case exhibits a nearly bounded iteration count that is lower in all cases than that achieved by even the coarsest conforming mesh. We note that the extension of the Schwarz method to the nonconforming case required the development of a nonconforming coarse-grid operator, which was done by allowing N to vary in the (Q,Q^T) routines and calling them with $N = 1$ during assembly of the linear finite elements that define the coarse problem.

5 Transitional Flow Example

We have used the techniques presented in the preceding sections to simulate several flows at transitional Reynolds numbers, including hairpin vortex formation in the wake of a hemispherical roughness element [33], heat transfer augmentation in grooved-flat channel configurations, and, most recently, transition in a model of an arteriovenous (AV) graft [21].

An AV graft is constructed of synthetic material from an artery to a vein to provide an access site for hemodialysis patients. AV grafts are

Table 2: Iteration Count for Cylinder Problem

	Conforming			Nonconforming		
K	93	372	1488	77	308	1232
iter	68	107	161	50	58	60

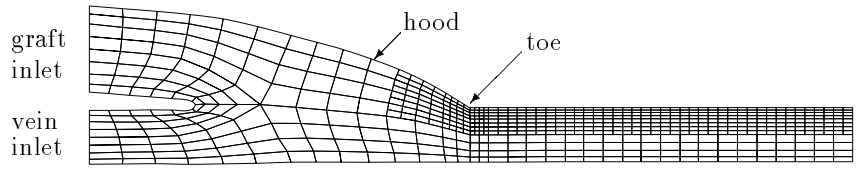

Figure 8: Symmetry-plane slice through nonconformig AV graft mesh.

unique in the vasculature in that their high flow-rates, which are necessary for efficient hemodialysis, can result in transition to turbulence that is often identified by an audible or palpable thrill downstream of the graft. This site is commonly associated with subsequent stenosis (narrowing) of the vein and, ultimately, graft failure. Understanding the cause of graft failure requires detailed knowledge of the hemodynamic environment in the vicinity of the AV graft juncture.

For purposes of validation, our initial investigations have focused on the end-to-side graft geometry illustrated in Fig. 8. Using the image-to-mesh translation procedure developed in [22], we obtained the computational mesh from an MRI scan of an upscaled Sylgard model (7.6 $\times$ *in vivo* scale) used for LDA experiments [21]. The graft axis intersects the host vein axis at an angle of 5°. Poiseuille flow is assumed at the graft and vein inlets. The ratio of the graft to vein diameter is 1.6:1, and the ratio of the graft to vein flow-rate is 9:1. The Reynolds number, Re, is based on the mean

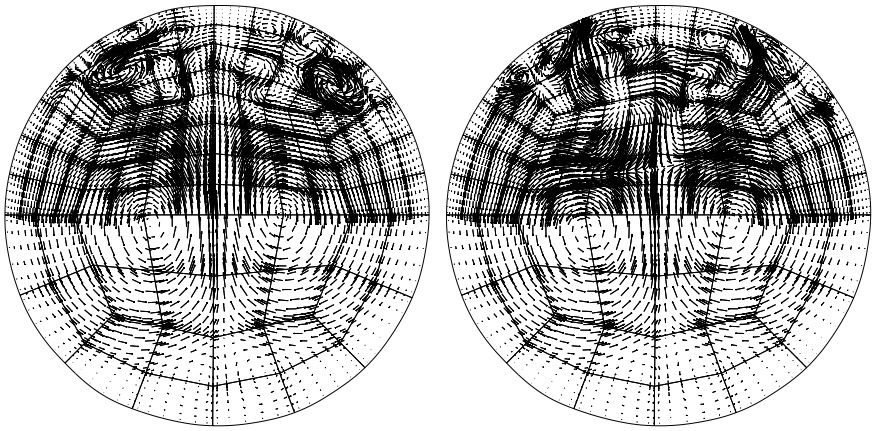

Figure 9: In-plane instantaneous velocity vectors at vein cross-sections located (left) 4.48 and (right) 4.64 vein diameters downstream from the toe of the graft.

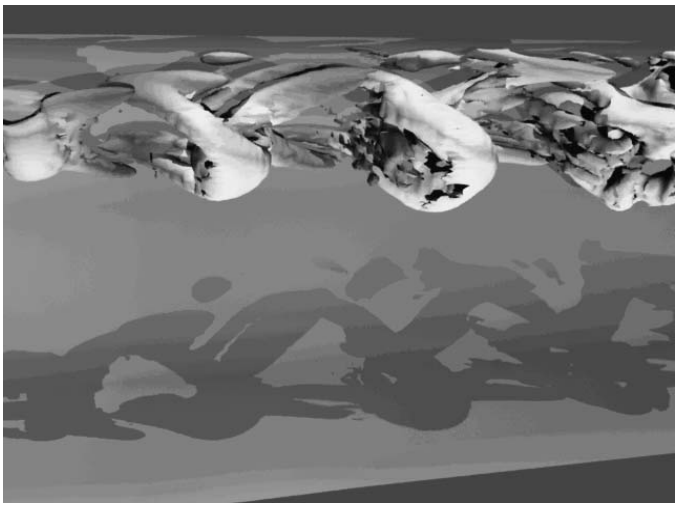

Figure 10: Coherent structures downstream of graft toe at Re=1820.

flow velocity and diameter at the graft inlet. The Reynolds number in the downstream venous segment is thus $Re_v = (1.6/.9)Re$.

Computations at Re=1820 were based on the nonconforming mesh of Fig. 8, with $K = 6168$ and $N = 7$, approximately 2,150,000 velocity points. Several features of the complex flow field are revealed in Fig. 9, which shows instantaneous in-plane velocity vectors at two axial slices downstream of the toe. First, there is significant bilateral symmetry because of the symmetric geometry and inflow conditions. The impact of nonsymmetric inlet conditions has been studied by Sherwin et al. [31]. Second, we observe a pair of large persistent vortices cutting across the horizontal midplane. These are Dean vortices that are set up as the parabolic graft-inlet flow impinges on the graft hood and is deflected downward. Third, there are many small-scale features in the upper half, including a pair of strong counter-rotating vortices near the vein wall at $x = 4.48$.

The small-scale structures are the result of the break-up of the shear layer that is formed as the flow enters the vein from the graft and separates from the vein wall (see Fig. 11). As illustrated in Fig. 10, the break-up leads to a sequence of periodically shed vortices that have a topology similar to the hairpin vortices observed in [33]. These vortices are identified by using the λ_2 criterion of Jeong and Hussain [19]. The colors mapped onto the λ_2 isosurfaces represent pressure. For a 6 mm graft, the shedding frequency is roughly 715 Hz, which is commensurate with both *in vivo* and *in vitro*

measurements described in [21].

We present in Fig. 11 a comparison with the laser Doppler anemometry measurements taken in the graft symmetry plane by Arslan [2]. The time-averaged velocity vectors (u_{avg}) reveal that both the experimental and numerical models have roughly the same size recirculation zone. However, the experimental profile recovers more quickly as the flow moves downstream. The profiles of the rms temporal fluctuations for the axial (u_{rms}) and vertical (v_{rms}) components clearly delineate regions of steady and unsteady flow. The spectral element method correctly predicts the axial and vertical location of the transition onset, as indicated by the first nonzero rms profiles downstream of the toe, as well as the magnitude of the disturbance.

6 Conclusion

We have presented a stabilized nonconforming spectral element formulation capable of accurate simulations of transition in complex domains. We have shown that the mesh geometry can have a significant impact on the conditioning of the underlying linear systems and that the nonconforming discretization can lead to improved meshes and consequent reductions in iteration count. Results for flow in an AV graft illustrate the potential of this approach for simulation of transition in complex geometries.

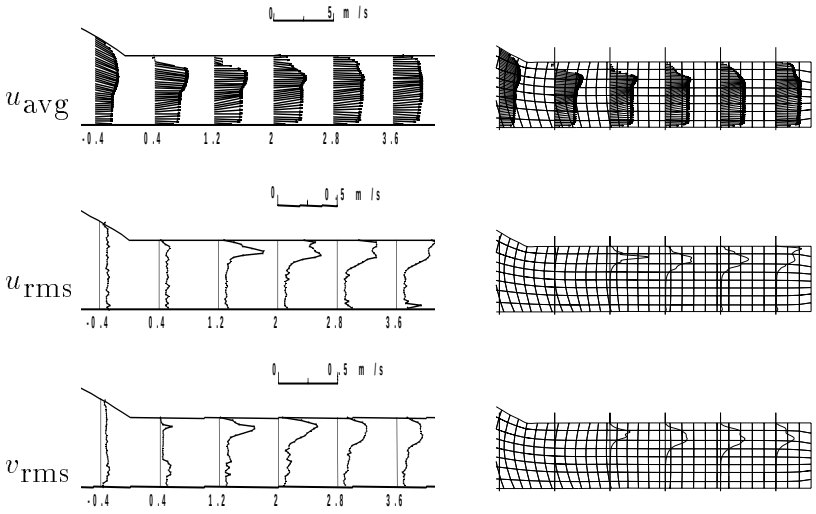

Figure 11: Velocity distributions at $Re = 1820$: LDA (left), SEM (right).

Acknowledgments

The authors thank Seung Lee and Henry Tufo for assistance with the AV graft simulations. This work was supported by the Mathematical, Information, and Computational Sciences Division subprogram of the Office of Advanced Scientific Computing Research, U.S. Department of Energy, under Contract W-31-109-Eng-38, and by the Faculty Research Participation program, administered by the Division of Educational Programs, Argonne National Laboratory.

References

[1] G. Anagnostou, Y. Maday, C. Mavriplis, and A. T. Patera. "On the mortar element method: Generalizations and implementation," in *Third International Symposium on Domain Decomposition Methods for Partial Differential Equations*, T. F. Chan, R. Glowinski, J. Périaux, and O. B. Widlund, eds., SIAM, pp. 157–173 (1990).

[2] N. Arslan, "Experimental Characterization of Transitional Unsteady Flow inside a Graft-to-Vein Junction," Ph.D. Thesis, Dept. of Mech. Eng., Univ. of Illinois, Chicago (1999).

[3] F. Ben Belgacem and Y. Maday "Nonconforming spectral element methodology tuned to parallel implementation" *Comp. Meth. Appl. Mech. Eng.*, **116**, pp. 59-67 (1994).

[4] C. Bernardi and Y. Maday. "Spectral methods," in P. G. Ciarlet and J. L. Lions, editors, *Handbook of Numerical Analysis*, **5** of *Techniques of Scientific Computing*, North Holland, pp. 209–486 (1997).

[5] J. P. Boyd, "Two comments on filtering for Chebyshev and Legendre spectral and spectral element methods," *J. Comp. Phys.*, **143**, pp. 283–288 (1998).

[6] D. L. Brown and M. L. Minion, "Performance of under-resolved two-dimensional incompressible flow simulations," *J. Comp. Phys.*, **122**, pp. 165–183 (1995).

[7] C. Canuto, "Spectral methods and the maximum principle," *Math. Comp.* **51**, 184, pp. 615–629 (1988

[8] C. Canuto, A. Russo, and V. Van Kemenade, "Stabilized spectral methods for the Navier-Stokes equations: Residual-free bubbles and preconditioning," *Comput. Methods Appl. Mech. Engrg* **166**, pp. 65–83 (1998).

[9] M. Casarin, "Schwarz Preconditioners for Spectral and Mortar Finite Element Methods with Applications to Incompressible Fluids," Ph.D. Thesis, *Technical Report* 717, Dept. of Computer Science, Courant Institute (1996).

[10] M. Dryja and O. B. Widlund, "An additive variant of the Schwarz alternating method for the case of many subregions," Technical Report 339, Dept. of Computer Science, Courant Institute (1987).

[11] P. F. Fischer, "Projection techniques for iterative solution of $A\underline{x} = \underline{b}$ with successive right-hand sides," *Comp. Meth. in Appl. Mech.*, **163**, pp. 193–204 (1998).

[12] P. F. Fischer, "An overlapping Schwarz method for spectral element solution of the incompressible Navier-Stokes equations," *J. Comp. Phys.*, **133**, pp. 84–101 (1997).

[13] P. F. Fischer, N. I. Miller, and H. M. Tufo. "An overlapping schwarz method for spectral element simulation of three-dimensional incompressible flows," in *Parallel Solution of Partial Differential Equations*, P. Bjorstad and M. Luskin, eds., Springer-Verlag, Berlin pp. 158–180 (2000).

[14] P. F. Fischer and J. S. Mullen, "Filter-based stabilization of spectral element methods," *Comptes Rendus de l'Acadmie des sciences Paris*, t. 332, - *Série I - Analyse numérique*, pp. 265-270 (2001).

[15] D. Funaro. "A new scheme for the approximation of advection-diffusion equations by collocation," *SIAM J. Numer. Anal.*, **30**, pp. 1664–1673 (1993).

[16] D. I. Gottlieb and S. A. Orszag. *Numerical Analysis of Spectral Methods: Theory and Applications*. SIAM-CBMS, Philadelphia, 1977.

[17] D. I. Gottlieb and J. S. Hesthaven. "Spectral methods for hyperbolic problems," *J. Comp. & Appl. Math.* **128**, pp. 83-131 (2001).

[18] R. D. Henderson and G. E. Karniadakis. "Unstructured spectral element methods for simulation of turbulent flows," *J. Comput. Phys.*, **122**, pp. 191–217 (1995).

[19] J. Jeong and F. Hussain, "On the identification of a vortex," *J. Fluid Mech.*, **285**, pp. 69–94 (1995).

[20] G. W. Kruse, "Parallel Nonconforming Spectral Element Methods," Ph.D. Thesis, Division of Applied Mathematics, Brown University (1997).

[21] F. Loth, N. Arslan, P. F. Fischer, C. D. Bertram, S. E. Lee, T. J. Royston, R. H. Song, W. E. Shaalan, and H. S. Bassiouny, "Transitional Flow at the Venous Anastomosis of an Arteriovenous Graft: Potential Relationship with Activation of the ERK1/2 Mechanotransduction Pathway," *preprint* (2001).

[22] S. E. Lee, N. Piersol, F. Loth, P. Fischer, G. Leaf, B. Smith, R. Yedevalli, A. Yardimci, N. Alperin, and L. Schwartz, "Automated Mesh Generation of an Arterial Bifurcation Base upon *in vivo* MR Images," presented at the World Congress on Medical Physics and Bioengineering, Chicago, IL (2000).

[23] Y. Maday and A. T. Patera, "Spectral element methods for the Navier-Stokes equations," in *State of the Art Surveys in Computational Mechanics*, A. K. Noor, ed., ASME, New York, pp. 71–143 (1989).

[24] Y. Maday, A. T. Patera, and E. M. Rønquist, "An operator-integration-factor splitting method for time-dependent problems: application to incompressible fluid flow," *J. Sci. Comput.*, **5**(4), pp. 263–292 (1990).

[25] Y. Maday, S. Ould Kaber, and E. Tadmor, "Legendre pseudospectral viscosity method for nonlinear conservation laws," *SIAM J. Numer. Anal.*, **30**, pp. 321–342 (1993).

[26] C. A. Mavripilis. "Non Conforming Discretizations and a posteriori Error Estimations for Adaptive Spectral Element Techniques," Ph.D. Thesis, Massachusetts Institute of Technology, Cambridge, MA (1989).

[27] S.A. Orszag. "Spectral methods for problems in complex geometry," *J.Comput. Phys.*, **37**, pp. 70–92 (1980).

[28] J. B. Perot, "An analysis of the fractional step method," *J. Comput. Phys.*, **108**, pp. 51–58 (1993).

[29] A. Quarteroni and A. Valli. *Numerical Approximation of Partial Differential Equations*. Springer Series in Computational Mathematics. Springer, Berlin, (1994).

[30] E. M. Rønquist, "Convection treatment using spectral elements of different order," *Int. J. Num. Methods in Fluids*, **22**, pp. 241–264 (1996).

[31] S. J. Sherwin, O. Shah, D. J. Doorly, J. Peiro, Y. Papaharilaou, N. Watkins, C. G. Caro, and C. L. Dumoulin, "The influence of out-of-plane geometry on the flow within a distal end-to-side anastomosis," *ASME J. Biomechanical Eng.*, **122**, pp. 1–10 (2000)

[32] E. Tadmor "Convergence of the spectral viscosity method for nonlinear conservation laws," in *11th International Conference on Numerical Methods in Fluid Dynamics*, Lecture Notes in Physics, **323**, D. L. Dwoyer, M. Y. Hussaini, and R. G. Voigt, eds., Springer-Verlag, , pp. 548–552 (1989).

[33] H. M. Tufo, P. F. Fischer, M. E. Papka, and K. Blom, "Numerical simulation and immersive visualization of hairpin vortices," presented at Supercomputing '99, Portland, OR, preprint ANL/MCS-P779-0899, Argonne National Laboratory (1999).

[34] T. A. Zang, N. Gilbert, and L. Kleiser, "Direct numerical simulation of the transitional zone," in *Instability and Transition, Vol. II*, ICASE/NASA LaRC Series, Y. Hussaini and R. Voigt, eds., Springer-Verlag, pp. 283–299 (1990).